

1 **Spherulite crystallization induces Fe-redox redistribution in silicic melt**

2  
3 Jonathan M. Castro<sup>1\*</sup>, Elizabeth Cottrell<sup>1</sup>, Hugh Tuffen<sup>2</sup>, Amelia Logan<sup>1</sup>, and Katherine  
4 A. Kelley<sup>3</sup>

5  
6 <sup>1</sup>Department of Mineral Sciences, Smithsonian Institution, 10<sup>th</sup> and Constitution Ave.  
7 NW, Washington, DC 20560

8  
9 <sup>2</sup>Department of Environmental Science, Lancaster University, LA1 4YQ, UK

10  
11 <sup>3</sup>Graduate School of Oceanography, University of Rhode Island, Narragansett, RI 02882

12  
13 \*Corresponding author: email: [castroj@si.edu](mailto:castroj@si.edu); phone: 202-633-1810; fax: 202-357-  
14 2476

15  
16 **Abstract**

17  
18 Rhyolitic obsidians from Krafla volcano, Iceland, record the interaction between mobile  
19 hydrous species liberated during crystal growth and the reduction of ferric iron in the  
20 silicate melt. We performed synchrotron  $\mu$ -FTIR and  $\mu$ -XANES measurements along a  
21 transect extending from a spherulite into optically distinct colorless and brown glass  
22 zones. Measurements show that the colorless glass is enriched in OH-groups and  
23 depleted in ferric iron, while the brown glass shows the opposite relationship. The color  
24 shift between brown and clear glass is sharp, suggesting that the colorless glass zone was  
25 produced by a redox front that originated from the spherulite margin and moved through  
26 surrounding melt during crystallization. We conclude that the most likely reducing agent  
27 is hydrogen, produced by magnetite crystallization within the spherulite. The Krafla flow  
28 dramatically captures redox disequilibrium on the microscale and highlights the  
29 importance of hydrous fluid liberation and late stage crystallization to the redox signature  
30 of glassy lavas.

31  
32 *Keywords:* Obsidian, spherulite, oxidation-reduction, FTIR, iron, hydrogen, XANES

33

34 **1. Introduction**

35

36 The chemical and physical processes in magma are influenced by the concentration and  
37 reaction of hydrogen-bearing components in the silicate melt. It is well known that the  
38 concentrations of molecular H<sub>2</sub>O and OH<sup>-</sup> groups, hereafter referred to collectively as  
39 “water”, dissolved in magma govern the positions of mineral liquidus curves and melt  
40 viscosities; both rise dramatically, resulting in crystallization (e.g., Geschwind and  
41 Rutherford, 1995) and melt stiffening (Hess and Dingwell, 1996), as magma degasses.  
42 The relationship between water and the ratio of ferric to ferrous iron in silicate melts  
43 remains an active area of research. In H<sub>2</sub>-buffered systems, the dissociation of water  
44 (e.g., H<sub>2</sub>O → H<sub>2</sub> + 1/2O<sub>2</sub>, Mueller, 1971) controls oxygen fugacity (*f*O<sub>2</sub>); thus *a*H<sub>2</sub>O  
45 controls Fe<sup>3+</sup>/Fe<sup>2+</sup>. The effect of water as a chemical component at fixed P, T, and *f*O<sub>2</sub> is  
46 more nuanced. The study of (Baker and Rutherford, 1996) suggested that the Fe<sup>3+</sup>/Fe<sup>2+</sup>  
47 ratio increased with the addition of water; however, as discussed by Wilke et al. (2005)  
48 and Gaillard et al. (2001), the study of Baker and Rutherford was not at constant oxygen  
49 fugacity (*f*O<sub>2</sub>). Experimental studies on rhyolite (Moore et al., 1995) and basalt  
50 (Botcharnikov et al., 2005) indicate that water, as a chemical component in a melt held at  
51 fixed T, P, and oxygen fugacity (*f*O<sub>2</sub>), has no effect on the Fe<sup>3+</sup>/Fe<sup>2+</sup> ratio. By contrast,  
52 other experimental studies indicate that as the bulk water content in increases so too does  
53 the Fe<sup>3+</sup>/Fe<sup>2+</sup> in the melt (Gaillard et al., 2001; Gaillard et al., 2003b). The relationship  
54 between water and iron redox state in natural magmas is thus an important factor to  
55 consider when reconstructing redox history of degassing magma (e.g., Mathez, 1984;  
56 Burgisser and Scaillet, 2007) or deciphering the oxidation states of magma source regions

57 (e.g., Carmichael, 1991).

58 Most natural magmas crystallize and vesiculate during their ascent towards and  
59 emplacement at the Earth's surface. Because these phase transformations redistribute and  
60 ultimately release volatile components from the system, they can drive oxidation-  
61 reduction (redox) reactions that will alter the speciation of iron in the magma.

62 Crystallization of silicate minerals that preferentially incorporate ferrous iron in their  
63 structures, such as olivine and pyroxene, result in a relatively oxidized melt residuum.

64 The manner by which crystallization of non-ferrous minerals such as quartz and feldspar  
65 affects the residual melt redox state is currently unknown; however, because these phases  
66 are anhydrous, their growth must redistribute water in the melt (Castro et al., 2008;  
67 Watkins et al., 2009), thereby influencing the chemical environment of iron (Gaillard et  
68 al., 2003c).

69 The release of H<sub>2</sub> from magma, either through its continuous outward diffusion or  
70 by liberation of H<sub>2</sub> gas in bubbles is widely thought to oxidize lavas (e.g., Sato and  
71 Wright, 1966; Sato, 1978; Mathez, 1984; Candela, 1986; Christie et al., 1886; Holloway,  
72 2004). The diffusive transport of hydrogen out of the melt (*m*) and into bubbles (*v*)  
73 displaces the following equilibrium to the right:  $2\text{FeO}_{(m)} + \text{H}_2\text{O}_{(m)} = \text{H}_{2(v)} + \text{Fe}_2\text{O}_{3(m)}$ .

74 Crystallization of magnetite may similarly alter the oxidation state of basaltic and silicic  
75 systems by the "auto-oxidation" reaction as defined by Holloway (2004):



77 The net effect of this reaction on system redox will be determined by the degree to  
78 which H<sub>2</sub> gas exits the system. If the hydrogen escapes the magmatic system completely  
79 (e.g. to bubbles or the atmosphere), the system is left relatively oxidized. If the hydrogen

80 is retained within the system, however, it may generate relatively reducing fluids adjacent  
81 to the zone of crystallization as proposed by Holloway (2004). Here we report adjacent  
82 zones of oxidation and reduction in the Krafla flow on a scale of only hundreds of  
83 microns.

84 In this paper, we describe fine-scale optical and chemical patterns in obsidian that  
85 link spherulitic plagioclase, quartz, and magnetite crystallization to reduction of ferric  
86 iron in the rhyolitic melt (Fig. 1). We show that reduced, colorless glass rims jacketing  
87 spherulites could have been produced by the expulsion of molecular water from growing  
88 spherulites, followed by crystallization of magnetite and concomitant production of  
89 hydrogen. The result is a boundary layer of reduced melt that grows with time. Given  
90 the considerable sizes ( $>1$  m; Smith et al., 2001) and high volume proportions of  
91 spherulites in many rhyolitic lavas and ignimbrites ( $\sim 90$  vol.%; Stevenson et al., 1994;  
92 Tuffen and Castro, 2009; Tuffen et al., in Review) the interplay of crystallization and  
93 micro-scale redistribution of oxidation states has important implications for the evolution  
94 of spherulite-rich lavas.

## 95 **2. Geological Background**

96 Spherulites are radiating, often concentrically arranged crystalline aggregates set  
97 in a glassy matrix (Fig. 1). They occur in obsidian domes, vitrophyric ash-flow tuffs  
98 (e.g., Smith et al. 2001), large-volume rhyolite flows such as those at Yellowstone (e.g.,  
99 Wright, 1915), and in shallow volcanic conduits (e.g., Stasiuk et al. 1996; Tuffen and  
100 Castro, 2009). Spherulites nucleate and grow in response to large undercoolings ( $>$   
101  $200\mu\text{C}$ ) rapidly imposed on the magma by its degassing and quenching (e.g., Swanson et  
102 al., 1989). As dictated by the thermal profile of a magma body (Manley, 1992; Tuffen et

103 al., in Review), spherulitic obsidian develops in spatially restricted zones (e.g., Manley  
104 and Fink 1987; Stevenson et al. 1994), comprising a transitional facies that separates the  
105 rapidly quenched, outermost vitrophyric rhyolite from a devitrified microcrystalline core.

106 Anomalously high volatile contents exist within and just above the spherulitic  
107 zones in lava domes (e.g., Westrich et al. 1988). Castro et al. (2008) have recently shown  
108 that the OH<sup>-</sup> concentrations in glass around spherulites are elevated above the background  
109 level. They interpreted these OH<sup>-</sup> concentration gradients to reflect the combined  
110 advection and diffusion of H<sub>2</sub>O away from the growing spherulites and numerically  
111 modeled these processes in order to estimate crystallization timescales. While their work  
112 confirms that spherulite crystallization drives volatile enrichment in silicic glass, it  
113 neither identifies the specific form of hydrous species ejected from the growing  
114 spherulite, nor constrains why an iron redox shift, manifested as a sharp color difference  
115 in the obsidian matrix (Fig. 1), is superimposed on the OH<sup>-</sup> concentration gradient in the  
116 glass. In this paper, we use microscopic chemical and textural evidence collected from  
117 the same sample studied by Castro et al. (2008) to demonstrate that regions of elevated  
118 OH<sup>-</sup> are linked to zones of iron reduction in the glass surrounding spherulites. This in  
119 turn suggests that spherulite growth may cause changes in the Fe-valence state in rhyolite  
120 melt.

### 121 **3. Analytical and experimental techniques**

122 All analyses were made on a decimeter-sized obsidian sample collected from the  
123 Hrafninnuhryggur ridge system on Krafla volcano, Iceland (Tuffen and Castro, 2009).  
124 Spherulite mineralogy was determined by 1) microscopic observation, 2) sample  
125 magnetism to identify Fe-oxides as magnetite, and 3) compositional data from energy

126 dispersive spectra (EDS) collected on a FEI NOVA nanoSEM600 FEG Variable Pressure  
127 Scanning Electron Microscope at the Smithsonian Institution National Museum of  
128 Natural History, operated at 7-12 KeV, 5 mm working distance and beam current ranging  
129 from 0.5-1 nA.

130 Major element glass compositions were analyzed using a JEOL JXA-8900R  
131 electron microprobe (EPMA) running software with ZAF corrections at the Smithsonian  
132 National Museum of Natural History. Analyses were performed with an acceleration  
133 voltage of 15 keV, a 10  $\mu\text{m}$  beam, and a 10 nA beam current. Standardization was  
134 performed on the following natural mineral standards: Quartz (Si), Anorthite (Ca),  
135 Bytownite (Al), Microcline (K), Albite (Na), Hornblende (Fe, Mg). A natural rhyolitic  
136 glass (VG568, Obsidian Cliffs, Yellowstone, USA) of known major element composition  
137 was periodically analyzed to check for instrument drift.

138 Determination of ferrous iron content was via wet chemical analysis of a  
139 powdered (grain size~180  $\mu\text{m}$ ) obsidian aliquot chipped from the same mass of sample  
140 on which all other measurements and observations were made. We attempted to separate  
141 out spherulite fragments from the glass powder. However, some glass-encrusted  
142 spherulites may have been over looked. Furthermore, it was not possible to separate the  
143 thin, clear glass halos from the pervasive brown glass. Thus, these measurements provide  
144 an average FeO concentration for the bulk brown glass with very minor dilution by the  
145 clear glass fraction. A total of nine (9) analyses were performed following the technique  
146 of Peck (1964) with some minor modifications in order to minimize oxidation during  
147 sample digestion. Digestion began in 8 ml of fluoroboric acid ( $\text{HBF}_4$ ) for 30 minutes in  
148 the ultrasonic bath. We then added 5 ml HF and 2 ml extra of  $\text{HBF}_4$  to the solution and

149 completed the digestion under heat for approximately 10 minutes. Three ferrous iron  
150 determinations were also made on the U.S.G.S. Glass Mountain Rhyolite standard RGM-  
151 1, which yielded a mean value of 1.19 wt. % FeO +/- 0.03 (1 $\sigma$ ). The nominal value for  
152 RGM-1 is 1.18 wt. % FeO.

153 H<sub>2</sub>O concentrations were determined by synchrotron-FTIR at the Advanced Light  
154 Source, Lawrence Berkeley National Laboratory. Measurements were made along  
155 traverses oriented perpendicular to the spherulite-glass boundaries on a Thermo Nicolet  
156 Magna 760 FTIR spectrometer interfaced with a NicPlan IR microscope (at beamline  
157 1.4.3). The IR beam has a diffraction-limited diameter of about 3  $\mu$ m. The uncertainty in  
158 spot position is  $\pm$  2  $\mu$ m. Transmittance spectra were obtained over the mid-IR (1,400-  
159 4,000 cm<sup>-1</sup>) to the near-IR (3,700-6,500 cm<sup>-1</sup>) regions with MCT detectors, KBr beam-  
160 splitters, and the synchrotron light source. 128 scans were used to obtain each spectrum  
161 and these spectra were corrected by subtracting a background spectrum collected every  
162 hour. We determined OH<sup>-</sup> concentrations from the intensity of the broad 3,570 cm<sup>-1</sup>  
163 absorption band, utilizing an absorption coefficient of 100 L mol<sup>-1</sup>cm<sup>-1</sup> (Newman et al.  
164 1986). We estimate the analytical uncertainty of OH<sup>-</sup> concentration to be  $\pm$  10% of the  
165 measured value.

166 The oxidation state of Fe in the glass was determined at the microscale using Fe  
167 K-edge X-ray Absorption Near Edge Structure ( $\mu$ -XANES) spectroscopy. The area-  
168 weighted average energy of the two pre-edge peaks, or centroid, shifts to higher energy as  
169 the ratio of ferric to ferrous iron increases, allowing quantification of Fe<sup>3+</sup>/ $\Sigma$ Fe in silicate  
170 glasses (e.g. Berry et al., 2003, Wilke et al., 2005, Cottrell et al., in press). Commensurate  
171 with this, the intensity of the peak corresponding to Fe<sup>3+</sup> (at higher energy) grows

172 proportionately larger relative to the intensity of the peak corresponding to  $\text{Fe}^{2+}$  (at lower  
173 energy); thus the ratio of peak intensities can also be used to quantify oxidation state  
174 (Wilke et al., 2005, Cottrell et al., in press).

175 Spectra were collected in fluorescence mode using a 9 element Ge array detector  
176 and a silicon channel-cut (311) monochromator at station X26A (bending magnet) at the  
177 National Synchrotron Light Source (NSLS), Brookhaven National Lab. The spot size on  
178 the sample was  $9 \times 5 \mu\text{m}$ . Spectra were recorded from 7020-7220eV with a 0.1eV step  
179 over the pre-edge from 7106-7118eV at 5s dwell. The pre-edge was deconvolved from  
180 the background absorption edge by simultaneously fitting the background with a damped  
181 harmonic oscillator function plus a line constrained to have a positive slope and the pre-  
182 edge features with two Gaussian peaks. The oxidation state of the glass was quantified  
183 using the empirical calibrations in Cottrell et al. (in press) based on pre-edge peak  
184 intensity ratios measured on a series of 16 basalt reference glasses with  $\text{Fe}^{3+}/\Sigma\text{Fe}$  ratios  
185 (0.088-0.601) independently determined by Mössbauer spectroscopy and 7 rhyolitic  
186 glasses with  $\text{Fe}^{3+}/\Sigma\text{Fe}$  ratios (0.238-0.806) independently determined by wet chemistry  
187 (Moore et al., 1996).

188 We performed a heating experiment on Krafla obsidian in order to induce  
189 spherulite crystallization and determine if optical and chemical changes in neighboring  
190 melt could result from this crystallization. General experimental details are given here,  
191 while more detailed experimental methods are given in the appendix. We first heated a 2  
192 cm-edge-length obsidian cube in a split-chamber tube furnace to  $770^\circ\text{C}$  at a rate of  $65^\circ\text{C}$   
193  $\text{min}^{-1}$ . The sample was held at  $770^\circ\text{C}$  for 90 minutes. After this period of time, the cube  
194 was removed from the furnace and blasted with cold compressed air, which cooled it to

195 room temperature in about 3 minutes. We then extracted a thin (~225  $\mu\text{m}$ ), doubly  
196 polished wafer from the center of the cube and examined the glass and spherulites near  
197 the center of that wafer. We also measured a water concentration profile along a traverse  
198 extending from one of the spherulites in the wafer center. We performed a similar  
199 experiment at 870°C, but the hydrous melt adjacent to the spherulites vesiculated  
200 intensely, rendering comparisons between the experimentally heated and natural  
201 unvesiculated samples difficult. Due to a lack of obsidian starting material, we could not  
202 repeat the experiment at 770°C.

203

## 204 **4. Results**

### 205 *4.1 Analytical measurements*

206 Fig. 1a is a photomicrograph of a natural spherulitic obsidian wafer that is the  
207 subject of the measurements discussed in the following paragraphs. The spherulites in  
208 this sample are composed of plagioclase and quartz (~95 vol.%), and minor amounts of  
209 clinopyroxene (2-3 vol.%) and magnetite (<0.8 vol.%; Castro et al., 2008). All of the  
210 spherulites are enclosed in haloes of colorless to light brown glass, which separate them  
211 from the pervasive dark brown matrix glass. The transitions between brown and  
212 colorless glass tend to be sharp around the larger spherulites (radii>100  $\mu\text{m}$ ) whereas the  
213 boundaries are more diffuse around the smaller spherulites.

214 Fig. 1b shows a representative OH<sup>-</sup> concentration profile measured with  
215 synchrotron-FTIR by Castro et al. (2008). The area under the profile is proportional to  
216 the amount of OH<sup>-</sup> groups in the silicate glass surrounding the spherulite. Castro et al.  
217 showed that the OH<sup>-</sup> concentration increases with the spherulite size, and typically

218 matches the amount of water that would be ejected during complete crystallization of  
219 anhydrous minerals from a melt volume equal to that of the spherulite. Differences  
220 between the measured and predicted OH<sup>-</sup> contents show that some spherulites retained  
221 water during their growth, consistent with the presence of glass and microvesicles (Castro  
222 et al., 2008).

223 Table 1 shows representative major element glass compositions measured within  
224 and across the differently colored glass regions. These data show that the composition of  
225 glass in the colorless halo, the transitional zone, and the distal brown glass surrounding  
226 the spherulite in Fig. 1a are indistinguishable within analytical error. Most importantly,  
227 there is no discernable change in the total iron content as the spherulite-glass boundary is  
228 approached; i.e., glass color is not a function of the total iron content but rather the ratio  
229 of ferric to ferrous iron. Fig. 2 is a graph showing the major element compositions of  
230 glass along a line traverse emanating from the spherulite shown in Fig. 1a.

231 By analogy with glasses equilibrated experimentally under controlled  $fO_2$ , the  
232 color difference between the halo and distal glass in the natural sample was suspected to  
233 reflect the proportions of ferric and ferrous iron, with the darker brown glass having more  
234 ferric iron than the light-colored glass (Gaillard et al. 2002; Donald et al., 2006;  
235 Moriizumi et al., 2008). This hypothesis was confirmed with  $\mu$ -XANES measurements.  
236 Spectra were collected on the spherulite shown in figure 1a both within the clear glass  
237 rim, approximately 20  $\mu$ m from the spherulite-glass border, and in the far-field brown  
238 matrix glass where the OH<sup>-</sup> concentration flattens out, about 330 $\mu$ m from the spherulite  
239 edge. Figure 3ab shows the raw pre-edge spectra, model components, and total model  
240 fits to the spectra. The spectrum taken in the distal brown glass (spot 2) displays a

241 proportionately larger  $\text{Fe}^{3+}$  peak, indicative of a greater contribution from ferric iron. This  
242 can be seen even more clearly in figure 3c when the baseline subtracted spectra are  
243 superimposed. Quantitatively, the centroid (area-weighted average of the two pre-edge  
244 peaks) shifts to higher energy by 0.18 eV moving from the clear rim to the distal brown  
245 glass. Consistent with this, the ratio of pre-edge peak intensities (i.e.  $I(\text{Fe}^{3+})/I(\text{Fe}^{2+})$   
246  $I(\text{Fe}^{3+})/[I(\text{Fe}^{2+}) + I(\text{Fe}^{3+})]$ ) shift to reflect a greater contribution from ferric iron in the  
247 distal brown glass than in the halo, consistent with a relative change in the ratio of  
248  $\text{Fe}^{3+}/\sum\text{Fe}$  of 0.06. The  $\mu\text{XANES}$  results clearly indicate a difference in the relative Fe  
249 oxidation state of the two glass regions, with the clear glass halos demonstrably reduced  
250 relative to the brown matrix glass. The absolute ferric iron content determined for the  
251 distal brown glass ( $\text{Fe}^{3+}/\sum\text{Fe} = 0.23\pm 0.04$ ) compares favorably with, but is more reduced  
252 than, the wet chemical determination of  $\text{Fe}^{3+}/\sum\text{Fe} = 0.29\pm 0.02$ , whereas Fe in the clear  
253 brown glass is more reduced ( $\text{Fe}^{3+}/\sum\text{Fe} = 0.17\pm 0.04$ ).

254 Fig. 4 shows measurements of the widths of several colorless glass haloes versus  
255 their corresponding spherulite radii. Estimated uncertainties in rim widths, stemming  
256 from the diffuse nature of the glass color boundaries, are shown as vertical error bars.  
257 The nonlinear regression to the data is a power-law function relating rim width to  
258 spherulite radius. Also shown in Fig. 4 are the predicted reduction rim widths for each  
259 spherulite based on calculations using empirical relationship of Gaillard et al. (2003a),  
260 which relates reduction front position or width to hydrogen fugacity, temperature (800°C)  
261 and time. These model calculations will be discussed further below.

262

263 *4.2 Experimental results*

264 The optical character and OH<sup>-</sup> concentration of the heated obsidian are shown in  
265 Figs. 5 and 6. To aid comparisons with the natural state, we also include images of  
266 unheated spherulite-rim combinations collected on the spherulite shown in Fig.1. The  
267 transmitted-light photomicrographs were taken at the same illumination and focal depth,  
268 and the imaged wafers were about the same thickness.

269 The salient features and changes in the heated sample are: 1) thin, ~10 μm wide  
270 veneers of plagioclase (identified with EDS on an SEM) jacketed all spherulites in the  
271 sample, 2) thin brown fringes composed of glass, plagioclase, and magnetite crystals  
272 located just inboard of the plagioclase veneers, 3) the colorless glass rims brightened, and  
273 on their outer periphery, thin, light-brown glass zones developed that appear to have  
274 propagated toward the spherulites, 4) circumferential cracks formed parallel to the  
275 colorless-brown glass boundaries, in some cases directly on them, and 5) along many of  
276 these cracks, small, ~10-30 μm, “bubble-trains” grew, comprising groups of spherical  
277 (Fig. 5c) to nearly completely flattened vesicles (Fig. 5d).

278 The most apparent changes that occurred during the heating experiment were  
279 crystallization and brightening of the colorless haloes (Fig. 5a, b). That the  
280 crystallization was “new” is indicated by the fact that none of the unheated spherulites  
281 have a jacket of feldspar around them. The crystallization rate implied by the amount of  
282 new plagioclase ( $\sim 1.7 \times 10^{-9}$  m sec<sup>-1</sup>; ie., width of plagioclase veneer divided by the  
283 experiment time) is similar to the average value ( $\sim 1.9 \times 10^{-9}$  m sec<sup>-1</sup>) determined by Castro  
284 et al. (2008) from their diffusion models at 800°C.

285 The circumferential fractures and small vesicle trains resulted from processes  
286 occurring, respectively, below and above the rheological glass transition ( $T_g$ ). At the

287 given heating rate, the sample reached  $T_g$  ( $\sim 700^\circ\text{C}$ ; Castro et al., 2008) in  $\sim 10$  minutes.  
288 During this short time the glass may have fractured due to its greater thermal expansion  
289 compared to the mineral phases in the spherulite. If this were the case, then fractures  
290 formed in tension as the expanding glass pulled away from the spherulite. Once the  
291 fractures formed, and the glass passed through  $T_g$ , bubble nucleation occurred  
292 preferentially along the fractures, which channeled volatile components to the growing  
293 bubbles. The cracks apparently served as conduits for degassing of the volatile-enriched  
294 boundary layers. An FTIR profile (Fig. 6) measured across one of these fractures  
295 indicates that the dissolved  $\text{OH}^-$  content decreases in the vicinity of a fracture, suggesting  
296 degassing into that fracture.

297

## 298 **5. Mechanism of Fe-reduction during crystallization**

299 It is clear from the geometry of the colorless glass haloes, specifically their  
300 proportional increase in width with spherulite size (Fig. 4), and their mimicking of the  
301 spherulite shapes, that the colorless glass rims resulted from the growth of the spherulites.  
302 The  $\mu$ -XANES spectra indicate that some ( $\sim 5$ -7% absolute or 26% relative) of the ferric  
303 iron in the glass adjacent to the spherulites has been reduced to ferrous iron (Fig. 3). In  
304 this section we address how these redox changes could have occurred in light of the  
305 analytical and experimental evidence.

306 We first consider the possibility that the heterogeneous ferric-ferrous iron  
307 distribution in the glass is related to the cooling history. Metrich et al. (2006) showed  
308 that the ferric-ferrous ratio in peralkaline rhyolitic glass inclusions appeared to increase  
309 upon slow cooling over several hundred  $^\circ\text{C}$  in high temperature  $\mu$ -XANES experiments.

310 They attributed the apparent oxidation in XANES spectra upon cooling to a change in the  
311 coordination environment of iron; high temperature favors tetrahedrally coordinated  
312 ferrous iron while lower temperatures stabilize octahedrally coordinated ferric iron.  
313 Metrich et al conclude that the XANES spectra of slowly cooled samples will appear  
314 more oxidized due to this coordination shift. To account for the reduced halos in the  
315 spherulitic obsidian, the reduced halos would have had to cool much more rapidly than  
316 the more oxidized distal brown glass, which is physically unlikely because latent heat  
317 liberated from the growing spherulites would have slowed cooling of the melt adjacent to  
318 the spherulite (Tuffen et al., submitted). Moreover, the color change in the glass supports  
319 a real difference in the oxidation state of iron, not a coordination change. For these  
320 reasons, this mechanism was probably not important for the formation of the colorless  
321 rims.

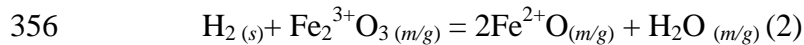
322 We next consider the possibility that the reduced-Fe signature in the rims arose  
323 from the late-stage crystallization of magnetite. The distribution of magnetite within  
324 spherulites, mainly as radial aggregates sandwiched between larger domains of  
325 plagioclase and quartz (Fig.1), suggests that magnetite grains formed in the latest stage of  
326 crystallization, from an interstitial melt that would have been enriched in water, further  
327 stabilizing magnetite (Sisson and Grove, 1993). Magnetite crystallization could act to  
328 reduce the melt adjacent to the spherulite via two potential mechanisms. First, hydrogen  
329 produced by magnetite crystallization in the presence of water (i.e., “auto oxidation,”  
330 reaction 1) would necessarily diffuse out of the spherulite, and would have subsequently  
331 reduced ferric iron in the neighboring melt. Second, magnetite crystallization alone will  
332 reduce iron in the glass residuum by virtue of its higher ferric/ferrous ratio (just as olivine

333 crystallization would raise the ferric/ferrous ratio). We show below that either  
334 mechanism, or both in concert, could have generated the reduced halos.

335 “Auto-oxidation” as described by Holloway (2004) may proceed in hydrous  
336 silicates when magnetite with a higher ferric/ferrous ratio than the melt from which it is  
337 crystallizing becomes stable. Pure end-member magnetite has a  $\text{Fe}^{3+}/\Sigma\text{Fe}$  of about 0.67,  
338 compared to the value of 0.22 - 0.29 in the brown glass; therefore magnetite precipitation  
339 could have resulted in “auto oxidation” in this hydrous lava from Krafla. In this scenario,  
340 magnetite precipitation proceeds through the consumption of water, generating one mole  
341 of  $\text{H}_2$  for every mole of magnetite crystallized (reaction 1). If  $\text{H}_2$  leaves the system  
342 completely through degassing along fractures, the remaining material is left relatively  
343 oxidized. As  $\text{H}_2$  diffuses through a melt, however, it necessarily results in a reduction  
344 front. We believe that these spherulites capture this disequilibrium state.

345 Simple mass balance arguments confirm the plausibility of this scenario. The  
346 modal proportion of magnetite in the spherulites, determined by BSE image analysis on  
347 10 different spherulites, is about 0.3 vol.% ( $\pm 0.12$ ). The amount of  $\text{Fe}^{3+}$  now residing in  
348 the magnetite grains within the large spherulite pictured in Fig. 1a is about 0.003 mg  $\text{Fe}^{3+}$   
349 ( $5.38 \times 10^{-8}$  moles of  $\text{Fe}^{3+}$ ), and because these magnetite grains contain some Ti (Castro  
350 et al., 2008), this estimate of  $\text{Fe}^{3+}$  in magnetite is a maximum. If all of the  $\text{Fe}^{3+}$  residing  
351 in the magnetite were created by oxidation of  $\text{Fe}^{2+}$  in the liquid, magnetite crystallization  
352 would produce a maximum of  $2.7 \times 10^{-8}$  moles of  $\text{H}_2$  via reaction (1). This hydrogen could,  
353 in turn, reduce  $5.38 \times 10^{-8}$  moles of ferric iron (i.e. 0.003 mg) in the adjacent melt (and  
354 produce water) according to:

355



357

358 Subscripts above refer to: (s)-spherulite and (m/g)-melt/glass. If all of the H<sub>2</sub>  
359 were transferred to the 100µm halo jacketing the spherulite in Figure 1a, it would shift  
360 the percentage of Fe<sup>3+</sup> from ~22% (measured via XANES) to 9%. We observe Fe<sup>3+</sup> in the  
361 halo equal to 16% (table 1), indicating that “auto-oxidation” within the spherulite could  
362 actually be responsible for iron reduction in the halo. This calculation is a maximum  
363 because it assumes that 100% of the ferric iron in the magnetite had to be converted from  
364 FeO (i.e. reaction 1). We observe, however, that the brown glass contains about 22%  
365 ferric iron. Assuming that reaction (1) proceeded at 78% efficiency (i.e. 22% of the ferric  
366 iron incorporated into the magnetite was already ferric), we still find that the percentage  
367 of Fe<sup>3+</sup> would drop to 11%. Within the error of the XANES measurements, the  
368 uncertainty of the reaction efficiency and mass balance, and even taking into account that  
369 the magnetite is Ti-bearing, this scenario remains plausible.

370 The auto-oxidation scenario is also corroborated by the high concentration of  
371 water in the halos. We observe the number of moles of “H<sub>2</sub>-equivalent” currently residing  
372 in the halo (i.e. one half the moles of OH<sup>-</sup>, calculated from the OH<sup>-</sup> concentration of  
373 0.19% measured by FTIR) equal to 5x10<sup>-8</sup>. This is ~45% higher than the number of  
374 moles of H<sub>2</sub> expected from magnetite crystallization via reaction (1). We therefore  
375 observe more “water” (hydroxyl and molecular) in the glass surrounding these spherulites  
376 than produced by magnetite crystallization. This “excess” water is expected because  
377 water is also rejected as an incompatible element in the growing spherulite (Castro et al.,  
378 2008).

379           A second mass-balance argument can be made that magnetite precipitation alone  
380 (i.e. not relying on the presence of water) could have caused the reduction halos.  
381 Magnetite incorporates iron in a ratio of  $2\text{Fe}^{3+}:1\text{Fe}^{2+}$ . Only 0.4% magnetite  
382 crystallization (as a percent of the glass now occupied by the reduced halos) is required to  
383 cause the ferric iron to decrease from ~22 to the observed value of ~16%. If we assume  
384 that all the magnetite seen in the spherulites crystallized from the volume of glass now  
385 occupied by the reduced halos, we observe 0.7% crystallization (which would reduce the  
386 ferric iron to 11%). If we assume that all of the magnetite seen in the spherulites  
387 crystallized from the volume of glass that now comprises the volume occupied by the  
388 spherulites plus the reduced halos, we observe 0.3% crystallization (which would reduce  
389 the ferric iron to 18%). These two values therefore bracket the maximum and minimum  
390 extents of magnetite crystallization, and either extreme provides a reasonable mechanism  
391 by which the glass in the halos could have been reduced. Crystallization of 0.4%  
392 magnetite from the halo would simultaneously cause the total iron concentration (FeO) in  
393 the halo to fall from 3.2 to 2.8%. This is close to within the error of the microprobe  
394 measurements. We have the added uncertainty of not knowing if the iron concentration  
395 could have been increased in the halo volume due to its incompatibility in early-  
396 crystallizing quartz and plagioclase. Nevertheless, no decrease or gradient in the iron  
397 concentration is observed in the halos relative to the distal brown glass. This, combined  
398 with the demonstrable presence of water in the system and the likelihood of the auto-  
399 oxidation reaction proceeding, leads us to slightly favor the auto-oxidation scenario as a  
400 means of generating the halos, but neither can be ruled out and in fact both could have  
401 contributed.

402 Gaillard et al. (2003a, c) simulated the process of hydrogen-flux iron reduction by  
403 exposing natural Fe-bearing rhyolitic melt and glass cylinders to reducing atmospheres of  
404 hydrogen and hydrogen-argon gas mixtures. Their experiments produced many of the  
405 features we observe around the natural spherulites: 1) a sharp change in glass color  
406 bounding a zone of reduced  $\text{Fe}^{3+}/\text{Fe}_{\text{total}}$  in hydrous glass, 2) sigmoidal  $\text{OH}^-$  concentration  
407 profiles emanating from the sample edge and attributable to hydrogen incorporation in  
408 the melt followed by diffusion of molecular water along the concentration gradient, and  
409 3) an offset between the reaction front position and the point of elevated  $\text{OH}^-$  in the glass.

410 Gaillard et al. (2003a, c) proposed that because hydrogen is very reactive with  
411 iron in the silicate melt, the reaction front progress in the melt is governed by the  
412 solubility and diffusion of hydrogen in the melt. The effective diffusion rate of  $\text{H}_2$ , in  
413 turn, was limited by the  $f\text{H}_2$  of their experiments. Gaillard et al. observed that the rate of  
414 progress of the reduction front ( $\mu\text{m}'\text{s}/\text{hour}$ ) was several orders of magnitude slower than  
415 the expected hydrogen diffusivity ( $\mu\text{m}'\text{s}/\text{sec}$ ) in the melt.

416 Gaillard et al. (2003a) performed time series experiments in order to characterize  
417 the rate of advancement of the reduction front with time. They observed a square-root-  
418 of-time dependence of the front position and, based on linear relationships between the  
419 square of the reduction front position and run duration, they extracted reduction rate  
420 constants,  $K=\mu^2/t$ , where  $\mu$  is the reaction front position, and  $t$  is time, for their  
421 experiments at  $800^\circ\text{C}$  and a range of hydrogen fugacities (0.02-50 bars). They proposed  
422 that the reduction rate was limited by hydrogen incorporation, which in turn, is a function  
423 of the fugacity-dependent  $\text{H}_2$  solubility and diffusivity in the melt.

424 It is possible that the spherulites behaved in a similar manner, that is, they acted

425 as hydrogen point sources to the neighboring melt. Although the boundary conditions are  
426 slightly different, e.g., the spherulites are an internal, as opposed to external hydrogen  
427 source, the empirical kinetic data of Gaillard et al. (2003c) can be used to assess whether  
428 the widths of the natural reduction rims are compatible with the timescales of spherulite  
429 growth. In other words, we assume that the reduction front started moving at the onset of  
430 spherulite growth and stopped when the growth ceased. By this simple scenario, the rim  
431 widths depend on the growth timescale, and therefore the duration that the expelled  
432 hydrogen had to react with the rhyolite melt according to the reaction rate constant  $K$   
433 (Gaillard et al. 2003a).

434 Castro et al. (2008) estimated average spherulite growth rates by modeling the  
435 combined advection and diffusion of water away from the growing spherulites and fitting  
436 model profiles to the natural  $\text{OH}^-$  concentration profiles. Even though their model did not  
437 account for hydrogen incorporation in the melt and its unknown effect on the kinetics of  
438  $\text{H}_2\text{O}$  diffusion, their growth rates match those determined experimentally on  
439 compositionally similar melts (e.g., Baker and Freda, 2001), and are probably accurate to  
440 an order of magnitude. According to their results at  $800^\circ\text{C}$  the spherulites grew at an  
441 average rate of  $\sim 10^{-9}\text{m/s}$  (Castro et al., 2008), which is similar to the rate determined in  
442 our spherulite growth experiments at  $770^\circ\text{C}$  (appendix).

443 Results of rim-width calculations are shown in Fig. 4. Individual spherulite  
444 growth timescales were determined by dividing the average growth rate ( $800^\circ\text{C}$ ; Castro et  
445 al., 2008) by their spherulite radii. Using the individual growth timescales ( $t$ ), we  
446 calculated rim widths ( $\mu$ ) using the relation  $\mu = (K \cdot t)^{1/2}$ . The best match between the  
447 calculated and natural rim widths was attained with the  $K$  value derived from the lowest

448 H<sub>2</sub> fugacity ( $f_{\text{H}_2}=0.02$  bar) in the experiments of Gaillard et al. (2003a). We found a very  
449 large mismatch at their next highest  $f_{\text{H}_2}$  (~0.25 bar H<sub>2</sub>) and attribute this to the nearly one  
450 order of magnitude increase in  $K$  at  $f_{\text{H}_2}=0.25$  bar, which translates to comparatively rapid  
451 rim growth relative to the spherulite growth timescales.

452 The agreement between the calculated and real Fe-reduction rim widths is good,  
453 suggesting that the natural rims could have developed under conditions of relatively low  
454 hydrogen fugacity (~0.02 bar according to Gaillard et al., 2003a). This match supports  
455 our hypothesis that it is molecular hydrogen that extrudes from the growing spherulite,  
456 thereby fluxing the ferric iron in the neighboring melt and causing the propagation of a  
457 redox front.

458

## 459 **6. Experimentally induced spherulite growth and Fe-reduction**

460 The experimental results of Gaillard et al (2003a, c) show that hydrogen fluxing  
461 of a silicate melt or glass will cause reduction of the ferric iron and the formation of a  
462 sharp reduction front that progresses with the square root of time. The close agreement  
463 between these experimental results and our natural observations suggests that the  
464 colorless haloes formed as a result of ferric iron reduction during spherulite growth, with  
465 hydrogen being a permissible reductant.

466

## 467 **7. Conclusion**

468 Our analysis indicates that the spherulitic growth of anhydrous phases can cause  
469 significant changes in Fe-oxidation state in the neighboring melt or glass around the  
470 growing crystals. Fe-redox reactions are driven by the liberation of hydrogen, and we

471 propose that it is hydrogen produced as a product of magnetite crystallization. The result  
472 is an Fe-reduction reaction that propagates through the glass or melt with time. That  
473 spherulite crystallization can cause reduction of ferric iron in the silicate melt suggests  
474 that this phenomenon could prevent oxidation of silicic lavas during their emplacement  
475 despite extensive crystallization. For example, Carmichael (1991) indicates that  
476 voluminous post-caldera rhyolite lavas at Yellowstone National Park, USA underwent  
477 little to no change in redox state compared to earlier-erupted ash flows. Carmichael  
478 (1991) used the apparent lack of oxidation of these lavas to support his hypothesis that  
479 “silicic magmas have redox states that reflect their source regions rather than H<sub>2</sub> loss.”  
480 He further explained that the low bulk H<sub>2</sub>O content of the post caldera lavas could have  
481 suppressed the activity of the H<sub>2</sub>O as most of the water would be speciated as OH groups  
482 (Stolper, 1982).

483 Spherulite crystallization is widespread in the interiors of the Yellowstone  
484 rhyolites (Wright, 1915; Colony and Howard, 1934), with some flows containing well  
485 over 50 vol.% spherulites (e.g., in the Nez Pierce flow). We suggest that the lack of  
486 variation in redox state may have been enabled by spherulite crystallization and local  
487 hydrogen solute rejection, but retention of generated hydrogen within the flows. Thus  
488 Carmichael’s (1991) conclusion that “silicic magmas with small amounts of iron and  
489 large amounts of water do not have their redox states reset” upon eruption may be a  
490 consequence of the offsetting effects of crystallization and glass reduction at the  
491 microscale.

492

493 **Acknowledgements**

494 We thank M.C. Martin for assistance with the SFTIR measurements and T. Gooding with  
495 sample preparation. Antonio Lanzirotti provided critical assistance at X26A, NSLS,  
496 Brookhaven National Lab. We thank F. Gaillard and M. Rutherford for valuable  
497 discussions. Finally, we appreciate the help of Landsvirkjun and the staff at Krafla power  
498 station during our sampling campaign in Iceland.

499

## 500 **References**

- 501 Bacon, C.R., Adami, L.H., Lanphere, M.A., 1989. Direct evidence for the origin of low  
502 <sup>18</sup>O silicic magmas: quenched samples of a magma chamber's partially-fused granitoid  
503 walls, Crater Lake, Oregon. *Earth and Planetary Science Letters* 96, 199-208.
- 504 Bajt, S., Sutton, S. R., Delaney, J. S., 1994. X-Ray Microprobe Analysis of Iron  
505 Oxidation-States in Silicates and Oxides Using X-Ray-Absorption near-Edge Structure  
506 (Xanes). *Geochimica Et Cosmochimica Acta* 58, 5209-5214.
- 507 Baker, D.R., Freda, C., 2001. Eutectic crystallization in the undercooled Orthoclase-  
508 Quartz-H<sub>2</sub>O system: experiments and simulations. *European Journal of Mineralogy* 13,  
509 453-466.
- 510 Baker, L.L., Rutherford, M.J., 1996. The effect of dissolved water on the oxidation state  
511 of silicic melts. *Geochimica et Cosmochimica Acta*, 60, 2179-2187.
- 512 Berry, A. J., O'Neill, H. S., Jayasuriya, K. D., Campbell, S. J. and Foran, G. J. (2003a).  
513 "XANES calibrations for the oxidation state of iron in a silicate glass." *American*  
514 *Mineralogist* **88**(7): 967-977.
- 515 Botcharnikov, R.E., Koepke, J., Holtz, F., McCammon, C., Wilke, M., 2005. The effect  
516 of water activity on the oxidation and structural state of Fe in a ferro-basaltic melt.  
517 *Geochimica Cosmochimica Acta*, 69, 5071-5085.
- 518 Burgisser, A., Scaillet, B., 2007. Redox evolution of a degassing magma rising to the

519 surface. *Nature* 445, 194-197, doi 10.1038/nature05509.

520 Candela, P.P., 1986. The evolution of aqueous vapor from silicate melts: Effect on  
521 oxygen fugacity. *Geochimica Cosmochimica Acta* 50, 1205-1211.

522 Carmichael, I.S.E., 1991. The redox states of basic and silicic magmas: a reflection of  
523 their source regions. *Contributions to Mineralogy and Petrology* 106, 129-141.

524 Castro, J.M., Beck, P., Tuffen, H., Nichols, A.R.L., Martin, M., 2008. Timescales of  
525 spherulite crystallization in obsidian inferred from water concentration profiles.  
526 *American Mineralogist* 93, 1816-1822.

527 Colony, R., Howard, A.D., 1934. Observations on spherulites. *American Mineralogist*  
528 19, 515-524.

529 Cottrell, E., Kelley, K. A., Lanzirrotti, A.T., Fischer, R. (submitted to *Chemical*  
530 *Geology*). High-Precision Determination of Iron Oxidation State in Silicate  
531 Glasses Using XANES.

532 Delaney, J. S., Dyar, M. D., Sutton, S. R., Bajt, S., 1998. Redox ratios with relevant  
533 resolution: Solving an old problem by using the synchrotron microXANES probe.  
534 *Geology* 26, 139-142.

535 Donald, S.B., Swink, A.M., Schreiber, H.D., 2006. High-iron ferric glass. *Journal of*  
536 *Non-crystalline Solids* 352, 539-543.

537 Gaillard, F., Scalliet, B., Pichavant, M., Beny, J-M., 2001. The effect of water and  $fO_2$  on  
538 the ferric-ferrous ratio of silicic melts. *Chemical Geology* 174, 255-273.

539 Gaillard, F., Scalliet, B., Pichavant, M., 2002. Kinetics of iron oxidation-reduction in  
540 hydrous silicic melts. *American Mineralogist* 87, 829-837.

541 Gaillard, F., Schmidt, B., Mackwell, S., McCammon, C., 2003a. Rate of hydrogen-iron

542 redox exchange in silicate melts and glasses. *Geochimica et Cosmochimica Acta* 67,  
543 2427-2441.

544 Gaillard, F., Pichavant, M., Scaillet, B., 2003b. Experimental determination of activities  
545 of FeO and Fe<sub>2</sub>O<sub>3</sub> components in hydrous silicic melts under oxidizing conditions.  
546 *Geochimica et Cosmochimica Acta* 67, 4389-4409.

547 Gaillard, F., Pichavant, M., Mackwell, S., Champallier, R., Scaillet, B., McCammon, C.,  
548 2003c. Chemical transfer during redox exchanges between H<sub>2</sub> and Fe-bearing silicate  
549 melts. *American Mineralogist* 88, 308-315.

550 Geschwind, C.H., Rutherford, M.J., 1995. Crystallization of microlites during magma  
551 ascent: the fluid mechanics of 1980-1986 eruptions at Mount St. Helens. *Bulletin of*  
552 *Volcanology* 57, 356-370.

553 Hess, K.U., Dingwell, D.B., 1996. Viscosities of hydrous leucogranitic melts: A non-  
554 Arrhenian model. *American Mineralogist* 81, 1297-1300.

555 Hildreth, W., Christiansen, R.L., O'Neil, J.R., 1984. Catastrophic isotopic modification  
556 of rhyolitic magma at times of caldera subsidence, Yellowstone Plateau volcanic field.  
557 *Journal of Geophysical Research* 89, 8339-8369.

558 Kress, V., Carmichael, I.S.E., 1991. The compressibility of silicate liquids containing  
559 Fe<sub>2</sub>O<sub>3</sub> and the effect of composition, temperature, oxygen fugacity and pressure on their  
560 redox states. *Contributions to Mineralogy and Petrology* 108, 82-92.

561 Manley, C. R., 1992. Extended cooling and viscous flow of large, hot rhyolite lavas:  
562 implications of numerical modeling results. *Journal of Volcanology and Geothermal*  
563 *Research* 53, 27-46.

564 Manley, C.R., Fink, J.H., 1987. Internal textures of rhyolite flows as revealed by

565 research drilling. *Geology* 15, 549-552.

566 Mathez, E.A., 1984. Influence of degassing on oxidation states of basaltic magmas.  
567 *Nature* 310, 371-374.

568 Métrich, N., Susini, J., Foy, E., Farges, F. Massare, D., Sylla, L., Lequien, S., Bonnin-  
569 Mosbah, M., 2006. Redox state of iron in peralkaline rhyolitic glass/melt: X-ray  
570 absorption micro-spectroscopy experiments at high temperature. *Chemical Geology*  
571 231, 350-363.

572 Moore, G., Righter, K., Carmichael, I.S.E., 1995. The effect of dissolved water on the  
573 oxidation state of iron in natural silicate liquids. *Contributions to Mineralogy and*  
574 *Petrology* 120, 170-179.

575 Moriizumi, M., Nakashima, S., Okumura, S., Yamanoi, Y., 2008. Color-change processes  
576 of a plinian pumice and experimental constraints on color-change kinetics in air of an  
577 obsidian. *Bulletin of Volcanology* DOI 10.1007/s00445-0080202-5.

578 Mueller, R.F., 1971. Oxidative capacity of magmatic components. *American Journal of*  
579 *Science* 270, 236-243.

580 Newman, S., Stolper, E.M., Epstein, S., 1986. Measurement of water in rhyolitic glasses:  
581 Calibration of an infrared spectroscopic technique. *American Mineralogist* 71, 1527-  
582 1541.

583 Northrup, Jr., C.J.M., Gerlach, T.M., Modreski, P.J., Galt, J.K., 1977. Potential fuel  
584 production from magma. Sandia National Laboratories Report SAND77-0509, 1-34.

585 Peck, L.C., 1964. Systematic analysis of silicates: U.S.G.S. Bulletin 1170, 80.

586 Sato, M., Wright, T.L., 1966. Oxygen fugacities directly measured in magmatic gases.  
587 *Science* 153, 1103-1105.

588 Sato, M. 1978. Oxygen fugacity of basaltic magmas and the role of gas-forming  
589 elements. *Geophysical Research Letters* 5, 447-449.

590 Sisson, T.W. and Grove T.L. 1993. Experimental investigations of the role of H<sub>2</sub>O in  
591 calc-alkaline differentiation and subduction zone magmatism. *Contributions to*  
592 *Mineralogy and Petrology*, 113, 143-166.

593 Smith, R.K., Tremallo, R.L., Lofgren, G.E., 2001. Growth of megaspherulites in a  
594 rhyolitic vitrophyre. *American Mineralogist* 86, 589-600.

595 Stasiuk, M.V., Barclay, J., Carroll, M.R., Jaupart, C., Ratte, J.C., Sparks, R.S.J., Tait,  
596 S.R., 1993. Degassing during magma ascent in the Mule Creek vent (USA). *Bulletin of*  
597 *Volcanology* 58, 117-130.

598 Stevenson, R.J., Briggs, R.M., Hodder, A.P.W., 1994. Physical volcanology and  
599 emplacement history of the Ben Lomond rhyolite lava flow, Taupo Volcanic Centre, New  
600 Zealand. *New Zealand Journal of Geology and Geophysics* 37, 345-358.

601 Stolper, E.S., 1982. The speciation of water in silicate melts. *Geochimica et*  
602 *Cosmochimica Acta* 46, 2609-2620.

603 Swanson, S.E., Naney, M.T., Westrich, H.R., Eichelberger, J.C., 1989. Crystallization  
604 history of Obsidian Dome, Inyo Domes, California. *Bulletin of Volcanology* 51, 161-  
605 176.

606 Tuffen, H., Castro, J.M., 2009. The emplacement of an obsidian dyke through thin ice:  
607 Hrafninnuhryggur, Krafla, Iceland. *Journal of Volcanology and Geothermal Research*.  
608 doi:10.1016/j.jvolgeores.2008.10.021.

609 Tuffen, H., Castro, J.M., Wilson, L., in Review. The thermal effects of spherulite  
610 crystallization in rhyolitic lava. *Earth and Planetary Science Letters*.

611 Watkins, J., Magma, M., Huber, C., and Martin, M., 2009. Diffusion-controlled  
612 spherulite growth in obsidian inferred from H<sub>2</sub>O concentration profiles. Contributions to  
613 Mineralogy and Petrology 157, 163-172.

614 Westrich, H.R., Stockman, H.W., Eichelberger, J.C., 1988. Degassing of rhyolitic  
615 magma during ascent and emplacement. Journal of Geophysical Research 93, 6503-  
616 6511.

617 Wilke, M., G. M. Partzsch, R. Bernhardt, Lattard, D., 2005. Determination of the iron  
618 oxidation state in basaltic glasses using XANES at the K-edge. Chemical Geology 220,  
619 143-161.

620 Wright, F.E., 1915. Obsidian from Hrafninnuhryggur, Iceland: Its lithophysae and  
621 surface markings. Bulletin of the Geological Society of America 26, 255-286.

622 Zhang, Y., Stolper, E.M., Wasserburg, G.J., 1991. Diffusion of water in rhyolitic glasses.  
623 Geochimica et Cosmochimica Acta 55, 441-456.

624

## 625 **Figure Captions**

626

627 **Figure 1.** A) Photomicrograph of spherulites (round and elliptical, black) in obsidian  
628 (brown). Various analytical points and traverses are shown (emp=electron probe  
629 microanalyzer; FTIR=Fourier Transform Infrared Spectroscopy; XANES=x-ray  
630 absorption near-edge spectroscopy). Black diamonds indicate approximate locations of  
631  $\mu$ -XANES measurements. Broader dark swaths are tracks left by a laser ablation ICPMS  
632 (these data are not discussed here). B) A back-scattered electron image showing typical  
633 internal spherulite texture. Bright phases are clinopyroxene and magnetite. C) An OH<sup>-</sup>  
634 concentration profile determined by FTIR collected along the lower right traverse in  
635 frame A. The vertical grey line is the approximate location of the colorless-brown glass  
636 boundary.

637

638 **Figure 2.** Major element compositions of glass leading up to a spherulite margin (at  
639 position = 0  $\mu$ m). All analyses were collected with an electron probe microanalyzer. The  
640 vertical grey bars demarcate the approximate ( $\pm 10$   $\mu$ m) position of the colorless-brown  
641 glass boundary.

642

643 **Figure 3.** Raw  $\mu$ -XANES spectra of the pre-edge region, model components, and model

644 fits for two points within the glassy matrix depicted in Figure 1A (a) Point 1 inside the  
645 colorless glass halo and (b) point 2 in the distal brown glass. (c) Model fits of the spectra  
646 in (a) and (b) baseline-subtracted and superimposed. Approximate positions of analysis  
647 points are shown on the inset photomicrograph. These data show the relative changes in  
648 ratio of  $\text{Fe}^{2+}$  to  $\text{Fe}^{3+}$  in the colorless and brown matrix glass. Iron in the glass near the  
649 spherulite (point 1) is significantly reduced compared to that in the far-field brown glass  
650 (point 2).

651

652 **Figure 4.** Colorless-glass rim width versus the apparent spherulite radius, measured on  
653 photomicrographs of the Krafla obsidian (solid dots). Error in rim width, shown as  
654 vertical bars, ranges from about 10-20%, and originates from the diffuse nature of the  
655 colorless-brown glass boundaries. Regression curve is a power law function of the form:  
656  $y=2x^{0.69}$ ;  $R^2=0.97$ . Solid triangles are the predicted rim widths based on the  
657 experimentally constrained hydrogen-iron reaction rate constant of Gaillard et al.  
658 (2003b), and the assumption that the rims developed during the interval of time that the  
659 spherulites grew, which in turn, is taken from the growth rate data of Castro et al. (2008).

660

661 **Figure 5.** Photomicrographs (500X; 200  $\mu\text{m}$  f.o.v.) collected on: A) a natural spherulite-  
662 glass combination, and B-D) an experimentally heated spherulitic obsidian. Frame A)  
663 shows the natural appearance of the spherulite margin (at top) and colorless and brown  
664 glass as viewed in transmitted, plane polarized light. The wafer is 197  $\mu\text{m}$  thick. Frame  
665 B) shows the typical appearance of the spherulite and colorless and brown glass after  
666 heating a similar piece of obsidian to 770 $\mu\text{C}$  for approximately 90 minutes. This wafer is  
667 about 202  $\mu\text{m}$  thick. Note the thin veneer ( $\sim 10 \mu\text{m}$ ) of plagioclase coating the spherulite  
668 margin (upper right) and the relative brightening of the colorless glass halo. Note also  
669 the crack running roughly in the center of the colorless halo with a string of small  
670 vesicles on its tip. Frame C) shows another view of the incipient crystallization and  
671 vesiculation that occurred during heat treatment. The vesicles here formed along an  
672 arcuate fracture in the colorless glass zone. Frame D) is a backscattered electron image  
673 of the three zones developed at the spherulite margin: the brown microlite rich fringe (a),  
674 plagioclase veneer (b), and the colorless and Fe-reduced matrix glass (c).

675

676 **Figure 6.** An  $\text{OH}^-$  concentration profile measured along a traverse extending from a  
677 spherulite in the heated obsidian sample. The position of traverse is shown on the  
678 subjacent photomicrograph. The vertical dashed and solid grey lines on the profile bound  
679 the light brown glass zone that may have formed as a result of degassing of hydrogen into  
680 the crack shown in the photomicrograph. Note the coincidence between the depression in  
681 the  $\text{OH}^-$  concentration profile and the position of the crack at  $\sim 75\text{-}80 \mu\text{m}$ .

682

683

684

685

686

687

688

689